Lidar multiple scattering factors inferred from CALIPSO lidar and IIR retrievals of semi-transparent cirrus cloud optical depths over oceans

Anne Garnier, Jacques Pelon, M. A. Vaughan, D. M. Winker, C. R. Trepte, P. Dubuisson

Atmos. Meas. Tech., 8, 2759–2774, 2015
www.atmos-meas-tech.net/8/2759/2015/
doi:10.5194/amt-8-2759-2015

Atmospheric Measurement Techniques
Open Access

Lidar multiple scattering factors inferred from CALIPSO lidar and IIR retrievals of semi-transparent cirrus cloud optical depths over oceans

A. Garnier[1], J. Pelon[2], M. A. Vaughan[3], D. M. Winker[3], C. R. Trepte[3], and P. Dubuisson[4]

[1]Science Systems and Applications Inc., Hampton, Virginia, USA
[2]Laboratoire Atmosphères, Milieux, Observations Spatiales, UPMC-UVSQ-CNRS, Paris, France
[3]NASA Langley Research Center, Hampton, Virginia, USA
[4]Laboratoire d'Optique Atmosphérique, Université Lille 1, Lille, France

Correspondence to: A. Garnier (anne.garnier@latmos.ipsl.fr)

Received: 31 December 2014 – Published in Atmos. Meas. Tech. Discuss.: 25 February 2015
Revised: 13 June 2015 – Accepted: 15 June 2015 – Published: 15 July 2015

Abstract. Cirrus cloud absorption optical depths retrieved at 12.05 µm are compared to extinction optical depths retrieved at 0.532 µm from perfectly co-located observations of single-layered semi-transparent cirrus over ocean made by the Imaging Infrared Radiometer (IIR) and the Cloud and Aerosol Lidar with Orthogonal Polarization (CALIOP) flying on board the CALIPSO (Cloud-Aerosol Lidar and Infrared Pathfinder Satellite Observations) satellite. IIR infrared absorption optical depths are compared to CALIOP visible extinction optical depths when the latter can be directly derived from the measured apparent two-way transmittance through the cloud. An evaluation of the CALIOP multiple scattering factor is inferred from these comparisons after assessing and correcting biases in IIR and CALIOP optical depths reported in version 3 data products. In particular, the blackbody radiance taken in the IIR version 3 algorithm is evaluated, and IIR retrievals are corrected accordingly. Numerical simulations and IIR retrievals of ice crystal sizes suggest that the ratios of CALIOP extinction and IIR absorption optical depths should remain roughly constant with respect to temperature. Instead, these ratios are found to increase quasi-linearly by about 40 % as the temperature at the layer centroid altitude decreases from 240 to 200 K. It is discussed that this behavior can be explained by variations of the multiple scattering factor η_T applied to correct the measured apparent two-way transmittance for contribution of forward-scattering. While the CALIOP version 3 retrievals hold η_T fixed at 0.6, this study shows that η_T varies with temperature (and hence cloud particle size) from $\eta_T = 0.8$ at 200 K to $\eta_T = 0.5$ at 240 K for single-layered semi-transparent cirrus clouds with optical depth larger than 0.3. The revised parameterization of η_T introduces a concomitant temperature dependence in the simultaneously derived CALIOP lidar ratios that is consistent with observed changes in CALIOP depolarization ratios and particle habits derived from IIR measurements.

1 Introduction

Cirrus clouds are widely distributed over the globe. Most cirrus exhibit compensating thermal and solar radiative effects, with the net effect depending on optical depth and particle size (Berry and Mace, 2014). Thus, well-validated global measurements of cirrus optical depths and properties are required to reliably assess their radiative impacts (Sassen et al., 2008). Ideally, these measurements would be validated using wholly independent retrievals from different instruments that use different measurement techniques having largely or wholly independent sources of uncertainty. While this multi-instrument approach is conceptually straightforward, there are typically a number of practical difficulties (e.g., accurate spatial and temporal matching) that make full realization of the technique somewhat challenging. The sensor design and selection for the Cloud-Aerosol Lidar and Infrared Pathfinder Satellite Observations (CALIPSO) mission (Winker et al., 2010) obviates most of these concerns. The instrumentation aboard the CALIPSO satellite includes CALIOP (the

Cloud and Aerosol Lidar with Orthogonal Polarization), a two-wavelength (532 and 1064 nm) polarization-sensitive (at 532 nm) elastic backscatter lidar (Hunt et al., 2009), a three-channel Imaging Infrared Radiometer (IIR) operating in the 8–12 µm thermal infrared spectral range (Corlay et al., 2000), and a wide field camera operating in the visible domain (Pitts et al., 2007). These instruments are assembled in a staring and near-nadir-looking configuration. The cross-track swaths of the passive sensors are centered on the lidar footprint so that observations from all three instruments are almost perfectly collocated in both time and space. The combined measurements thus allow highly detailed comparison studies that are not subject to collocation uncertainties or concerns about view angle differences.

CALIOP cirrus visible optical depths are total extinction optical depths retrieved using one of two different and totally independent techniques (Young and Vaughan, 2009). The first method is the so-called "constrained retrieval", in which the cloud optical depth is derived from the apparent two-way transmittance as measured from molecular scattering above and below the cloud layer using an instrument-specific correction for multiple scattering effects. Indeed, in case of cirrus clouds, composed of crystals that are very large compared to the CALIOP visible wavelength ($\lambda = 532$ nm), a significant fraction of the scattering energy is included in a small angle forward lobe and may stay in the lidar receiver field of view for an extended distance below the cloud base and hence contribute to an apparent increase of the measured two-way transmittance of the cloud. This fraction of energy varies with ice crystal phase function, ice crystal size, and lidar configuration (Nicolas et al., 1997; Chepfer et al., 1999; Hogan, 2008). The multiple scattering factor, η, introduced by Platt (Platt, 1973; Platt et al., 2002) is a convenient parameter to correct the apparent two-way transmittance for contribution from multiple scattering (Nicolas et al., 1997; Eloranta, 1998). In the single-scattering limit, η is equal to 1. In version 3 of the CALIOP algorithm, η is assumed constant throughout the layer, identical in cloud and below cloud, and equal to 0.6. The second method, called "unconstrained retrievals", is used when reliable measurements of the apparent two-way transmittance are not available. Optical depths derived using unconstrained retrievals use the same assumptions about η that are used in the constrained technique. In addition, a priori assumptions about the layer extinction-to-backscatter ratio, a quantity also known as the lidar ratio, S_{cal}, are also required. The accuracy of the optical depth estimates obtained in this manner depends critically on the accuracy of the assumed apparent lidar ratio S^*, which is defined as the product of S_{cal} and η.

Direct measurements of apparent two-way transmittance can also be obtained in the presence of some well-characterized secondary scattering layer lying beneath the cirrus. Among the secondary scattering targets that have been recently identified for use in constrained retrievals are ocean surfaces (Josset et al., 2012) and opaque water clouds (Hu et al., 2007). However, the only constrained retrieval target currently implemented in the standard CALIOP analyses is clear air. It has long been recognized that when the scattering characteristics of the ambient molecular atmosphere are well known (e.g., from models or rawinsonde measurements), the apparent two-way transmittance of a layer can be measured directly whenever sufficiently clean air is found immediately above and below the layer (Young, 1995; Elouragini and Flamant, 1996; del Guasta, 1998; Chen et al., 2002; Yorks et al., 2011). The main advantage of the constrained retrieval technique is that it does not require an a priori assumption about the apparent lidar ratio. On the contrary, because the layer apparent optical depth has been measured, accurate estimates of S^* can be retrieved by applying the constrained retrieval technique to suitable CALIOP data (Young and Vaughan, 2009; Young et al., 2013). Thus, the only assumed parameter in the constrained retrieval technique is the multiple scattering factor.

In order to extend the constrained approach, Platt (1973) proposed a combined radiometric and lidar retrieval to more fully characterize cirrus cloud properties. In this paper, the relationship between infrared absorption and visible extinction optical depth retrieved from CALIPSO is investigated in detail, based on heritage from the pioneering work of C. M. R. Platt in the 1970s, which is applied here to global space-borne observations. Previously, Lamquin et al. (2008) conducted a closely related study by combining infrared retrievals from Atmospheric Infrared Sounder (AIRS) with apparent optical depths retrieved by the authors from co-located CALIOP measurements. More recently, Josset et al. (2012) conducted a similar analysis using IIR data and apparent optical depth retrievals constrained by ocean surface measurements from both CALIOP and the CloudSat radar. Here, infrared absorption optical depths retrieved from IIR observations of single-layered cirrus clouds at 12.05 µm are compared to the visible optical depths derived by applying CALIOP's constrained retrieval technique to precisely collocated measurements of the same cloud. Based on a detailed analysis of these comparisons, a new relationship describing the temperature-dependent effect of multiple scattering in the CALIOP retrievals is derived and discussed. The technique used to retrieve cirrus emissivity and absorption optical depths from the CALIPSO IIR measurements is described in depth by Garnier et al. (2012a). A substantial review of this method is given below. These analyses use version 3 CALIOP Level 2 5 km cloud layer and profile products and the corresponding version 3 IIR Level 2 track products (Powell et al., 2013). The paper is constructed as follows. Retrieval techniques, sources of uncertainty, and expected ratios between retrievals in the visible and in the infrared are presented in Sect. 2. In the IIR algorithm, emissivity and absorption optical depth are retrieved assuming an isothermal cloud layer of equivalent temperature inferred from the CALIOP layer detection algorithm. This technique is assessed in Sect. 3. CALIOP and IIR retrievals are then

compared and discussed in Sect. 4. Using analyses organized around the specifics of each algorithm and cloud characteristics such as optical depth and temperature, the CALIOP multiple scattering factor derived from these comparisons is evaluated. Section 5 provides a summary of the work and presents our conclusions about the effectiveness of these multi-sensor analyses.

2 CALIPSO retrieval techniques

2.1 CALIOP

A detailed overview of CALIOP retrievals can be found in Winker et al. (2009) and the works cited therein. Here we provide only a brief synopsis. The CALIOP Level 1 calibrated 532 nm total attenuated backscatter profiles are used to detect scattering layers with horizontal resolutions of 5, 20, or 80 km, defined by the amount of averaging required to detect the layers (Vaughan et al., 2009). After discriminating between clouds and aerosols (Liu et al., 2009), cloud layers are further classified according to thermodynamic phase and crystal habit as water clouds, randomly oriented ice clouds, or horizontally oriented ice clouds (Hu et al., 2009). Cirrus cloud optical depths are then retrieved by CALIOP's Hybrid Extinction Retrieval Algorithms (HERA) (Young and Vaughan, 2009). Uncertainties in CALIOP optical depth retrievals are described extensively in Young et al. (2013).

When clear air is found immediately above and below a cirrus cloud layer, the apparent two-way transmittance can be obtained directly from the ratio of the mean attenuated scattering ratios, $\langle R' \rangle$, in clear air regions above and below the cloud; i.e., $T^2_{\text{apparent}} = \langle R' \rangle_{\text{below}} \big/ \langle R' \rangle_{\text{above}}$. The visible apparent optical depth is simply

$$\tau_{\text{apparent}} = \frac{-\ln\left(T^2_{\text{apparent}}\right)}{2}, \tag{1}$$

and the visible optical depth is

$$\tau_{\text{vis}} = \tau_{\text{apparent}} \big/ \eta, \tag{2}$$

where division by the multiple scattering factor η represents the required correction of the measured transmittance. These multiple scattering contributions are attributed solely to forward scattered photons that originate from in-cloud scattering events and subsequently propagate into the clear air below cloud base.

According to the equation introduced by Platt (1973), the apparent lidar ratio S^* can be derived from this apparent two-way transmittance as

$$S^* = \frac{1 - T^2_{\text{apparent}}}{2\gamma'} = \frac{1 - e^{-2\cdot\tau_{\text{apparent}}}}{2\gamma'} = \frac{1 - e^{-2\cdot\eta\tau_{\text{vis}}}}{2\gamma'}, \tag{3}$$

where γ' is the cloud attenuated backscatter vertically integrated between layer top and base altitudes. It is noted that Eq. (3) was established within cloud, so that η should be η_c to represent the in-cloud multiple scattering factor that is supposed to be constant with range. As discussed in Winker (2003), deriving S^* from Eq. (3) assumes that the multiple scattering factors within and below the cloud are identical – i.e., that $\eta = \eta_c$, whereas η below the cloud can be larger than η_c in cloud (Nicolas et al., 1997). The difference between S^* and the true in-cloud apparent lidar ratio, S_c*, can be estimated analytically from Eqs. (2) and (3) as

$$\frac{S^* - S^*_c}{S^*} = \frac{2\cdot\tau_{\text{apparent}}\cdot e^{-2\cdot\tau_{\text{apparent}}}}{1 - e^{-2\cdot\tau_{\text{apparent}}}} \cdot \frac{(\eta - \eta_c)}{\eta}. \tag{4}$$

As illustrated in Winker (2003), (S^*–S_c*) / S^* is identical to $(\eta - \eta_c) / \eta$ when optical depth tends to 0 and decreases as optical depth increases. Similarly, the analyses in this study will rely on apparent optical depths derived from apparent two-way transmittances, so that the inferred multiple scattering factor will be η below cloud. The lidar ratio S_{cal} will be derived from S^* after correction for multiple scattering as

$$S_{\text{cal}} = S^* \big/ \eta\,, \tag{5}$$

whereas the true in-cloud lidar ratio, $S_{\text{cal,c}}$, should be derived from Eq. (5), but using S^*_c and η_c. The difference between S_{cal} and $S_{\text{cal,c}}$ is estimated from Eqs. (4) and (5) as

$$\frac{S_{\text{cal}} - S_{\text{cal,c}}}{S_{\text{cal}}} = \frac{S^* - S^*_c}{S^*} - \frac{\eta - \eta_c}{\eta} = \left(\frac{2\cdot\tau_{\text{apparent}}\cdot e^{-2\cdot\tau_{\text{apparent}}}}{1 - e^{-2\cdot\tau_{\text{apparent}}}} - 1\right)\cdot\frac{(\eta - \eta_c)}{\eta}. \tag{6}$$

Here, the relative bias (S_{cal}–$S_{\text{cal,c}}$) / S_{cal} is 0 when optical depth tends to 0, and approaches progressively $-(\eta - \eta_c)/\eta$ as optical depth increases. As $\eta - \eta_c$ is ≥ 0, the lidar ratios derived from this technique can be too small, more notably for the largest optical depths. However, no information is available to us to quantify this bias.

In version 3 of the CALIOP data products, the HERA module identifies those layers for which constrained solutions are considered feasible by requiring that the estimated relative uncertainty in the derived lidar ratio be less than 40 % (Young and Vaughan, 2009). An initial estimate of S^* is then derived from Eq. (3) and is refined iteratively until the integral of the retrieved extinction profile exactly matches the directly determined apparent optical depth (Young and Vaughan, 2009). This relative uncertainty increases rapidly for small optical depths (Young et al., 2013) and during nighttime, constrained solutions are generally deemed not possible for optical depths typically smaller than 0.3. Because solar background illumination injects large amounts of noise into the CALIOP daytime backscatter signal, the signal-to-noise ratios needed to satisfy this rather stringent requirement are almost never found in CALIOP daytime measurements. As a consequence, CALIOP version 3 constrained retrievals are available almost exclusively during

nighttime for optical depths typically larger than 0.3. For consistency, optical depths reported in the CALIOP 5 km cloud layer product are derived from the measured apparent two-way transmittance using Eq. (2) only when the constrained technique is applied to retrieve the extinction profiles reported in the CALIOP cloud profile product. Otherwise, the optical depths reported in the version 3 layer product are retrieved using an initial lidar ratio set to $S_{\rm cal} = 25$ sr. Nevertheless, whenever the layer apparent two-way transmittance could be measured it is also reported, so that optical depth can also be computed a posteriori using Eq. (2), as for the constrained retrievals, hence extending the data set of measured apparent optical depths. In any case, the conversion of apparent optical depth into single-scattering optical depth depends on an a priori specification of the multiple scattering factor.

2.2 IIR

The IIR is a passive instrument providing calibrated radiances in three channels in the atmospheric window (8.65, 10.6, and 12.05 µm), with a medium spectral resolution of about 1 µm and a spatial resolution of 1 km per pixel over a 69 km swath. IIR channels are optimized for retrievals of cirrus optical and microphysical properties, such as ice crystals effective diameter (Garnier et al., 2012a, 2013). The IIR 12.05 µm channel, which exhibits the largest absorption by cirrus clouds, is chosen for this analysis. The pixels located at the center of the 69 km swath are precisely collocated with CALIOP lidar footprint, and thus a vertically resolved description of the atmospheric column associated with passive IIR observations is obtained from CALIOP active measurements. IIR retrievals rely on cloud and aerosol detections from CALIOP, and as IIR observations are not vertically resolved the most suitable scenes are those containing only one single cloud layer in the column. Scenes containing low opaque water clouds, also analyzed by the IIR algorithm, are not included in this study. In addition, scenes containing dense depolarizing aerosol layers such as mineral dust are discarded. They represent less than 1 % of the total number of scenes.

Cloud absorption is characterized through its emissivity ε as (Platt and Gambling, 1971; Platt, 1973; Garnier et al., 2012a)

$$\varepsilon = \frac{R_{\rm BG} - R_{\rm m}}{R_{\rm BG} - R_{\rm BB}}, \tag{7}$$

where $R_{\rm m}$ is the measured calibrated radiance, $R_{\rm BG}$ is the background radiance at the top of the atmosphere that would be observed in the absence of the studied cloud, and $R_{\rm BB}$ is the radiance of a blackbody source located at the cloud radiative altitude. Cloud absorption optical depth $\tau_{\rm a}$ is subsequently derived as

$$\tau_{\rm a} = -\ln(1-\varepsilon). \tag{8}$$

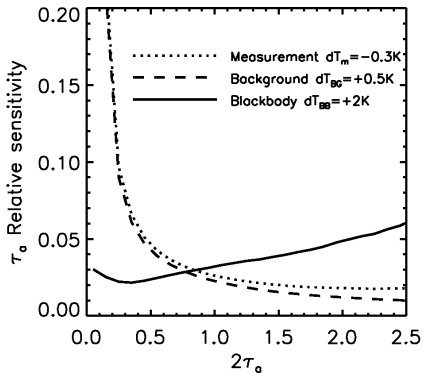

Figure 1. Relative sensitivity of absorption optical depth $\tau_{\rm a}$ to variations of measured (dotted), background (dashed), and blackbody (solid) brightness temperatures $dT_{\rm m} = -0.3$ K, $dT_{\rm BG} = 0.5$ K, and $dT_{\rm BB} = 2$ K, respectively.

Uncertainty in the emissivity includes three components associated with errors on $R_{\rm m}$, $R_{\rm BG}$, and $R_{\rm BB}$ and is inversely proportional to the radiative contrast $R_{\rm BG}$–$R_{\rm BB}$ (Garnier et al., 2012a). In other words, the colder the cloud with respect to the underlying scene, the smaller the uncertainty in the emissivity retrievals. It is convenient to introduce the error $dR\prime_x$ on the radiance R_x, where the subscript x refers to m, BB, or BG, further weighted by the inverse of the radiative contrast, so that

$$dR'_x = \frac{\partial R_x}{\partial T} \cdot dT_x \cdot \frac{1}{R_{\rm BG} - R_{\rm BB}}, \tag{9}$$

where dT_x is the error on the radiance R_x converted in terms of equivalent brightness temperature. Thus, the sensitivity $d\tau_{{\rm a},x}$ of $\tau_{\rm a}$ to an error dT_x can be simply written for each component:

$$d\tau_{\rm a,m} = \left(-1/1-\varepsilon\right) \cdot dR'_{\rm m} \tag{10a}$$

$$d\tau_{\rm a,BB} = \left(\varepsilon/1-\varepsilon\right) \cdot dR'_{\rm BB} \tag{10b}$$

$$d\tau_{\rm a,BG} = dR'_{\rm BG}. \tag{10c}$$

Uncertainty estimates are derived after assessing the random and systematic errors $dT_{\rm m}$, $dT_{\rm BG}$, and $dT_{\rm BB}$. As an illustration, Fig. 1 shows the relative sensitivity $d\tau_{{\rm a},x}/\tau_{\rm a}$ to $dT_{\rm m} = -0.3$ K, $dT_{\rm BG} = +0.5$ K, and $dT_{\rm BB} = +2$ K for cirrus clouds. The rationale for this choice of values is given below. The variation $d\tau_{\rm a,BG}$ due to a variation $dR'_{\rm BG}$ of the weighted background radiance does not depend on ε, and the relative variation $d\tau_{\rm a,BG}/\tau_{\rm a}$ (dashed line) decreases with $\tau_{\rm a}$, more rapidly for $2\tau_{\rm a}$ smaller than 0.3. A similar behavior is seen for the measured radiance (dotted line). However, the relative variation of $\tau_{\rm a}$ due to a variation of $dT_{\rm BB}$ increases steadily with $\tau_{\rm a}$ (solid line).

The on-board measured calibrated radiances have been validated by comparison with airborne observations (Sourdeval et al., 2012). Assuming that the measurement is not biased, a random noise $dT_{\rm m} = \pm 0.3$ K is considered based on

the noise equivalent differential temperature and calibration accuracy as assessed by the Centre National d'Etudes Spatiales (CNES).

Both R_{BG} and R_{BB} in Eq. (7) are inferred in synergy with CALIOP observations and so too are the respective uncertainty estimates dT_{BG} and dT_{BB} (Garnier et al., 2012a).

The background radiance, R_{BG}, is preferably retrieved from cloud-free observations in neighboring pixels along track as identified by CALIOP at a distance chosen to be smaller than 100 km from the analyzed pixel. The cloud layers for which these conditions are fulfilled are identified as "type 1 clouds". If these conditions are not found, R_{BG} is computed using the FASt RADiative (FASRAD) transfer model (Dubuisson et al., 2005) and ancillary atmospheric and surface data from the GEOS 5 model of the Global Modeling and Assimilation Office (Rienecker et al., 2008). This second ensemble of cloud layers is called "type 2 clouds". Type 1 and type 2 clouds will be evaluated separately as their sources of uncertainty are different. Indeed, for type 1 clouds, R_{BG} is derived purely from observations and is expected to be unbiased with respect to measured radiances. A random error dT_{BG} is assumed, which is arbitrarily augmented from the instrumental random noise $dT_m = \pm 0.3$ to ± 0.5 K to account for possible differences between the studied area and the nearby non-cloudy area.

The blackbody radiance R_{BB} is computed from the FASRAD model and the thermodynamic temperature, T_c, at the centroid altitude, Z_c, of the CALIOP attenuated backscatter profile at 532 nm within the cloud layer (Vaughan et al., 2005). This parameter, derived from Level 1 CALIOP observations, is reported in the CALIOP 5 km layer product and is available as an input to the IIR Level 2 operational algorithm. In order to assess possible systematic errors dT_{BB}, the cloud radiative temperature, T_r, can be computed a posteriori from CALIOP extinction profiles and compared with the temperature T_c. This analysis is detailed in Sect. 3. Subsequent systematic errors on IIR optical depth and corrections will also be discussed. An additional error of $dT_{BB} = \pm 2$ K is assumed to account for possible biases in the atmospheric model.

Even though the IIR analyses take advantage of spatial information (e.g., cloud heights) derived from CALIOP collocated vertical profile observations, the IIR cloud optical properties retrievals are entirely independent from the CALIOP optical properties retrievals. The measurement techniques used by the two sensors rely on different physical principles and hence are subject to very different sources of uncertainty. The expected relationship between CALIOP and IIR optical depths is presented in the following section.

2.3 Simulated relationships between CALIOP and IIR optical depths

Ratios of CALIOP cirrus visible extinction optical depth τ_{vis} to IIR absorption optical depth τ_a at 12.05 µm are simulated using the FASDOM radiative transfer model (Dubuisson et al., 2005, 2008) for an isothermal cloud and ice crystal optical properties retrieved from pre-computed tables (Yang et al., 2005). Figure 2 shows simulated τ_{vis}/τ_a ratios for clouds composed of hexagonal solid columns and of aggregates by taking $\tau_a = 0.25$. Effective diameters (D_e) (x axis) are defined as 3/2 times the ratio of volume to projected area (Mitchell, 2002). As seen in Fig. 2, τ_{vis}/τ_a increases as D_e increases for D_e larger than 10–15 µm, from 1.7–1.9 at D_e equal to 20 µm up to 2.07 at D_e equal to 140 µm. These simplified simulations, which assume mono-disperse particle size distributions, are sufficient to assess the sensitivity of τ_{vis}/τ_a to ice crystal size and habit and to establish that τ_{vis}/τ_a is expected to be around 2. A more detailed discussion is given in Sect. 4. It is to be noted that τ_a is not, strictly speaking, an absorption optical depth as it includes a small contribution from multiple scattering, which becomes more important as optical depth grows larger. Simulations show that τ_a is increased by less than 3 % with respect to pure absorption optical depth at τ_a equal to 1.25, or τ_{vis} around 2.5, which is the maximum value attained by the semi-transparent cirrus clouds considered in this study.

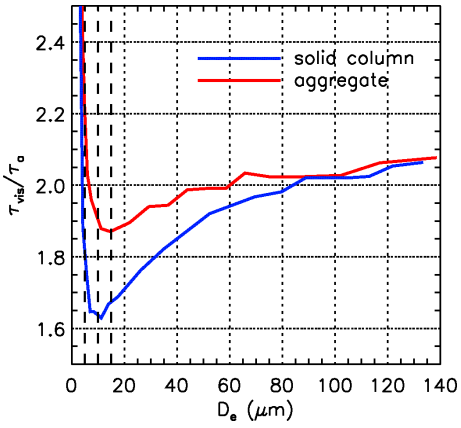

Figure 2. Simulations of the ratio between CALIOP optical depth at 532 nm (τ_{vis}) and IIR absorption optical depth at 12.05 µm (τ_a) at $\tau_a = 0.25$ against effective diameter D_e for hexagonal solid columns (blue) and aggregates (red). Vertical dashed lines indicate D_e smaller than 15 µm (see text).

3 Cloud radiative temperature

As seen in Sect. 2, cloud effective emissivity and hence infrared absorption optical depth are retrieved through a simple relationship (see Eq. 7) by considering an isothermal cloud of blackbody radiance R_{BB} computed using the centroid temperature T_c at the centroid altitude Z_c. In this section, systematic errors in the blackbody brightness temperature dT_{BB} resulting from this assumption are quantified. To do so, the cloud radiative temperature T_r is computed a posteriori from CALIOP extinction profiles and compared to T_c, so that ul-

timately IIR retrievals can be corrected using Eqs. (9) and (10b).

CALIOP extinction profiles are reported at 5 km horizontal resolution in the cloud profile products and are derived from the exact same attenuated backscatter profiles that are used to compute the centroid altitudes reported in the 5 km layer products. As the intent is to evaluate IIR retrievals, analyses are conducted for single-layered semi-transparent cirrus clouds over ocean. Data selection is further restricted to the subset of cirrus clouds composed of randomly oriented ice crystals for which the ice–water phase classification is reported with high confidence. In addition, possible contamination from mixed-phase clouds is minimized by restricting the analysis to clouds whose temperature at base altitude is colder than −20 °C (Hu et al., 2010). CALIOP optical depths and extinction profiles are retrieved from the constrained technique described previously. The chosen time period covers 12 months in 2008.

Each cloud is composed of a number, n, of vertical bins, i, of resolution δz, with $i = 1$ to $i = n$ extending from base to top. Emissivity in bin i is noted $\varepsilon(i)$ and absorption optical depth derived from Eq. (8) is $\tau_a(i)$. By applying Eq. (7) successively to each of the bins, from cloud base to cloud top, it is found that the cloud blackbody radiance R_{BB} can be expressed as

$$R_{BB} = \frac{\sum_{i=1}^{i=n} \varepsilon(i) \cdot R_{BB}(i) . e^{-\sum_{j=i+1}^{j=n+1} \tau_a(j)}}{\sum_{i=1}^{i=n} \varepsilon(i) \cdot e^{-\sum_{j=i+1}^{j=n+1} \tau_a(j)}}, \quad (11)$$

where $R_{BB}(i)$ is the blackbody radiance of bin i of thermodynamic temperature $T(i)$, and $\tau_a(n+1)$ represents absorption above the cloud.

The denominator in Eq. (11) represents the cloud emissivity. The cloud blackbody radiance can be seen as the centroid radiance of the attenuated emissivity profile, with the attenuation term corresponding to the infrared transmittance above the bin i. This expression has been validated by comparing R_{BB} from Eq. (11) and from the FASRAD model. In Eq. (11), absorption by gases such as water vapor and ozone in the cirrus cloud is neglected, so that absorption is assumed to be purely due to the cloud. This simplification has no impact on the result for τ_a larger than 0.2 and otherwise biases R_{BB} by only 0.4 K of equivalent brightness temperature when τ_a tends to 0. Assuming a ratio r between CALIOP visible optical depth τ_{vis} and IIR absorption optical depth τ_a, Eq. (11) can be rewritten as a function of the CALIOP cloud extinction coefficient α (in km^{-1}) and r as

$$R_{BB} = \frac{\sum_{i=1}^{i=n} \left(1 - e^{-[\alpha(i) \cdot \delta z / r]}\right) \cdot R_{BB}(i) . e^{-\sum_{j=i+1}^{j=n+1} [\alpha(j) \cdot \delta z / r]}}{\sum_{i=1}^{i=n} \left(1 - e^{-[\alpha(i) \cdot \delta z / r]}\right) \cdot e^{-\sum_{j=i+1}^{j=n+1} [\alpha(j) \cdot \delta z / r]}}. \quad (12)$$

The temperature T_r is derived from the blackbody radiance R_{BB} computed using Eq. (12). The ratio r is taken equal to 2 based on the simulations shown in Sect. 2.3, as well as 2 ± 0.4 to evaluate the sensitivity of R_{BB} to r. The vertical resolution δz is equal to 0.06 km in the CALIOP profiles products.

However, the centroid altitude Z_c can be written as

$$Z_c = \frac{\sum_{i=1}^{i=n} Z(i) \cdot \left(\beta_{part}(i) + \beta_{mol}(i)\right) \cdot e^{-2\sum_{j=i}^{j=n} [\eta \alpha_{part}(j) + \alpha_{mol}(j)] \cdot \delta z}}{\sum_{i=1}^{i=n} \left(\beta_{part}(i) + \beta_{mol}(i)\right) \cdot e^{-2\sum_{j=i}^{j=n} [\eta \alpha_{part}(j) + \alpha_{mol}(j)] \cdot \delta z}}, \quad (13)$$

where $Z(i)$ is the altitude of bin i, $\beta_{part}(i)$ and $\beta_{mol}(i)$ are, respectively, the particulate and molecular components of the total backscatter (in sr^{-1} km^{-1}), $\alpha_{part}(i)$ and $\alpha_{mol}(i)$ are, respectively, the particulate and molecular extinction coefficients (in km^{-1}), and η represents the required correction for multiple scattering introduced in Sect. 2.1. Equation (13) exhibits interesting similarities with Eq. (12). As radiance and altitude vary quasi-linearly with temperature within a few kilometer deep layer, Eqs. (12) and (13) are effectively two different weighted averages of the cloud temperature profile. In both cases, the weight is composed of the product of a transmittance term and of a multiplying term. For cirrus clouds of sufficient optical depth, the molecular contribution is weak compared to the particulate one, and the transmittance term in Eq. (13) is driven by $2\eta\alpha(j)$ or $1.2\alpha(j)$ assuming $\eta = 0.6$ for CALIOP observations, which is larger than $\alpha(j)/r$ in Eq. (12), or $\alpha(j)/2$ if $r = 2$. Thus, the smaller transmittance term in Eq. (13) compared to that in Eq. (12) tends to provide Z_c higher than the radiative cloud altitude for observations from the top of the atmosphere. However, this is partly compensated by the multiplying terms. Indeed, in Eq. (13) the multiplying term is roughly proportional to the bin absorption optical depth $\tau_a(i) = \alpha(i) \cdot \delta z / r$, because the lidar ratio is constant in CALIOP extinction retrievals (Young and Vaughan, 2009). Therefore, the multiplying term in Eq. (13) can be seen as $\tau_a(i)$, which is larger than the multiplying term in Eq. (12), i.e., the emissivity $\varepsilon(i)$.

Overall, the temperature T_r derived from Eq. (12) is found to be warmer than the temperature T_c derived from Eq. (13) as seen in Fig. 3a, where mean T_r–T_c differences are plotted against $2\tau_a$ for several ranges in cloud geometric thicknesses Δz from 1–2 km up to 7–8 km (colored lines) and for all observations (black line). The T_r–T_c differences represent systematic errors dT_{BB} on the blackbody brightness temperature used in the IIR standard retrievals. They are primarily driven by the cloud geometric thickness Δz and increase quasi-linearly with optical depth ($2\tau_a$) for a given Δz. The slope is close to 0 for the smallest thicknesses, Δz in 1–2 km, and increases up to 1.5 K per unit optical depth for Δz in 7–8 km. On average, the bias increases with $2\tau_a$ (black curve) from 0.5 to 3 K because optical depth and geometric thickness are not fully independent. Standard deviations are between 0.2 and 1.5 K (Fig. 3b) and include variability due to the fact that T_r–T_c varies with the shape of the extinction profile for a given optical depth and a given geometric thickness.

Biases shown in Fig. 3a have been retrieved assuming an a priori value $r = 2$. Sensitivity to this assumption is seen

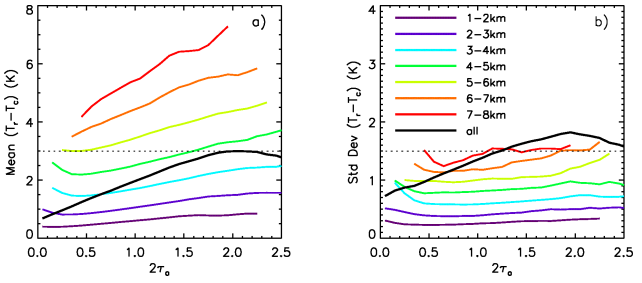

Figure 3. (a) Mean value and **(b)** standard deviation of the difference T_r–T_c between cloud radiative temperature and temperature at centroid altitude of attenuated total backscatter against $2\tau_a$ assuming $r = \tau_{vis} / \tau_a = 2$. Colored lines are for several ranges in cloud geometric thickness. The black line is for all samples. The horizontal dotted lines indicate maximum values discussed in the text. Data set: single-layered cirrus randomly oriented ice with high confidence, base temperature < −20 °C, over ocean, 2008.

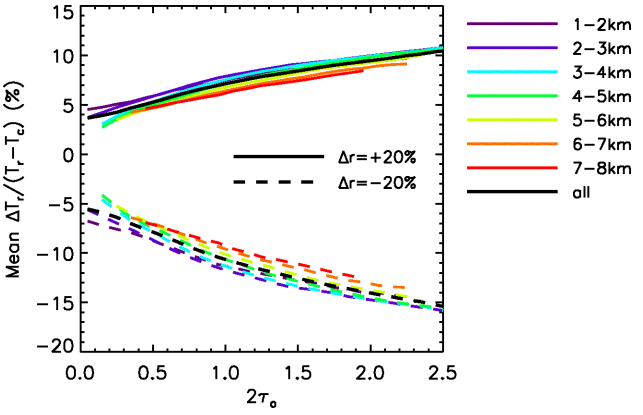

Figure 4. Relative sensitivity (in percentage) of the difference T_r–T_c to a variation of $\Delta r = +20\,\%$ (solid lines) and $\Delta r = -20\,\%$ (dashed lines) of the assumed τ_{vis} / τ_a ratio $r = 2$. Colored lines are for several ranges in cloud geometric thickness Δz .The black lines are for all samples. Same data set as in Fig. 3.

in Fig. 4, showing relative variations $\Delta T_r / (T_r – T_c)$ of T_r–T_c when r is changed to 2.4 ($\Delta r = +20\,\%$, solid lines) and to 1.6 ($\Delta r = -20\,\%$, dashed lines), to cover a range of possible values according to the simulations (Fig. 2). As will be shown in Sect. 4, assuming r between 1.6 and 2.4 also allows coverage of the range of retrieved values. Increasing the ratio $r = \tau_{vis} / \tau_a$ does decrease τ_a as τ_{vis} is set from CALIOP retrievals, and the radiative temperature is increased ($\Delta T_r / (T_r – T_c)$ is positive). The opposite behavior is found when the ratio r is decreased. The estimated bias $dT_{BB} = T_r – T_c$ shown in Fig. 3a for $r = 2$ is found to vary by less than 16 % in the worst case, which is for $2\tau_a = 2.5$ and $\Delta r = -20\,\%$, with small variations with respect to geometric thickness. Therefore, the bias dT_{BB} is estimated and corrected in the following by taking $r = 2$.

Correcting for a bias dT_{BB} ranging between 0.5 K at $2\tau_a \approx 0$ and 7 K at $2\tau_a = 2$ as seen in Fig. 3a induces a relative increase of τ_a between 0.5 and 17 % according to Fig. 1 and, on average, the largest increase is 7 % for $dT_{BB} = 3$ K at $2\tau_a = 2$. In the following, CALIOP and IIR retrievals will be compared before and after correcting IIR absorption optical depths for those biases in order to assess the impact on the comparisons.

4 Comparison of IIR and CALIOP retrievals

CALIOP and IIR cirrus retrievals are evaluated through ratios of CALIOP visible optical depth τ_{vis} to IIR absorption optical depth τ_a. Data selection is the same as in Sect. 3. IIR absorption optical depths, reported at 1 km pixel resolution under the lidar track in the IIR Level 2 track products, are averaged to a 5 km horizontal resolution to match the resolution at which CALIOP optical depth is reported in the CALIOP 5 km cloud layer products. Median τ_{vis} / τ_a ratios during 2008 in the 25° S–25° N latitude band are plotted against $2\tau_a$ in Fig. 5. Figure 5a is from the standard products whereas Fig. 5b is obtained with τ_a corrected by using the cloud blackbody radiance R_{BB} derived from CALIOP extinction profiles as described in Sect. 3. In order to simultaneously evaluate biases due to the background radiance R_{BG} as presented in Sect. 2, results are plotted by segregating type 1 clouds, for which a measured R_{BG} is available and used to retrieve τ_a (solid lines), from type 2 clouds, for which R_{BG} is from computations (dashed lines). Furthermore, retrievals from computed R_{BG} are also plotted for type 1 clouds (dotted lines) for comparison with the standard retrievals (solid line). Finally, the τ_{vis} / τ_a ratios are shown for several ranges in centroid temperature T_c. Figure 5c shows the number of samples used to build the statistics. The standard deviation of the τ_{vis} / τ_a ratios plotted in Fig. 5d is found similar when τ_a is from standard products or corrected for the cloud radiative temperature. Figure 5 shows that the median τ_{vis} / τ_a ratios are overall within the ranges of expected values according to the simulations shown in Fig. 2. Figure 5 also contains pieces of information about systematic errors on IIR and CALIOP retrievals, which are discussed first. The retrieved τ_{vis} / τ_a ratios and their variations with T_c as seen in both Fig. 5a and b are discussed afterwards. Tropics are chosen for this discussion for simplicity, because biases due to computed R_{BG} are known to vary with latitude (Garnier et al., 2012a), but this does not affect the representativeness of the results.

4.1 Systematic errors: IIR

The τ_{vis}/τ_a ratios derived for type 1 clouds from measured R_{BG} (Fig. 5, solid lines) are expected to be the most accurate because they are the most constrained by IIR observations. For these exact same clouds, τ_a from computed R_{BG} (dotted lines) differs from τ_a from measured R_{BG} (solid line) by less than 2 % at $2\tau_a = 0.7$. As, according to Fig. 1, an error $dT_{BG} = 0.5$ K induces a relative error in τ_a equal to 3.5 % at $2\tau_a = 0.7$, this indicates a bias $dT_{BG} = 0.3$ K in the computations. However, as seen in Sect. 3, the correction of R_{BB} increases τ_a and as expected, the τ_{vis}/τ_a ratios in Fig. 5b are smaller than in Fig. 5a. For type 1 clouds, it is seen that the corrected R_{BB} decreases the τ_{vis}/τ_a ratio by less than 5 % for the largest optical depths.

Type 1 and type 2 clouds are mutually exclusive and appear to have different properties. As seen in Fig. 5c, the fraction of type 2 clouds is larger at colder temperatures and the number of type 1 clouds is not significant at 193–203 K. Type 2 clouds are found to represent more than 85 % of the analyzed clouds in the western Pacific, in the Indian Ocean, and in the Atlantic Ocean and to represent 76 % overall in the tropics. Type 1 clouds are expected to be isolated cloud systems of small horizontal dimension or at the edge of large systems, whereas type 2 clouds are expected to be embedded in large cloudy areas. This is consistent with the fact that most of the type 1 clouds have a geometric thickness Δz between 1.5 and 3 km whereas type 2 clouds are deeper, with Δz mostly between 3 and 6 km and up to 8 km (not shown). Therefore, the blackbody correction is overall larger for type 2 clouds than for type 1 ones (Fig. 3a). As a result, a better agreement between τ_{vis}/τ_a from type 1 (dotted lines) and from type 2 (dashed) clouds is clearly noted after correction (Fig. 5b) than before correction (Fig. 5a) for the largest $2\tau_a$ between 1 and 1.5. After correction, the overall difference between τ_{vis}/τ_a from type 2 and from type 1 clouds is $+1$ to $+5$ % at $2\tau_a = 0.7$, which is possibly due to additional biases of -0.2 to -0.8 K (Fig. 1) in the computed R_{BG}, even though actual differences of the τ_{vis}/τ_a ratios cannot be ruled out because two distinct ensembles of clouds are compared. Further analyses of the differences between observations and computations are being conducted to help inform and improve future versions of the IIR science data products.

The τ_{vis}/τ_a ratio exhibits a sharp decrease of about 40 % from $2\tau_a = 0.3$ to $2\tau_a = 0.5$ for each temperature range and decreases slowly by about 10 % from $2\tau_a = 0.7$ to $2\tau_a = 2.5$. This behavior is observed for both type 1 and type 2 clouds. Because for type 1 clouds (solid lines) R_{BG} is from neighboring observations, biases in IIR τ_a retrievals do not seem to be a tenable explanation. As a consequence, possible biases in CALIOP retrievals are investigated in the following section.

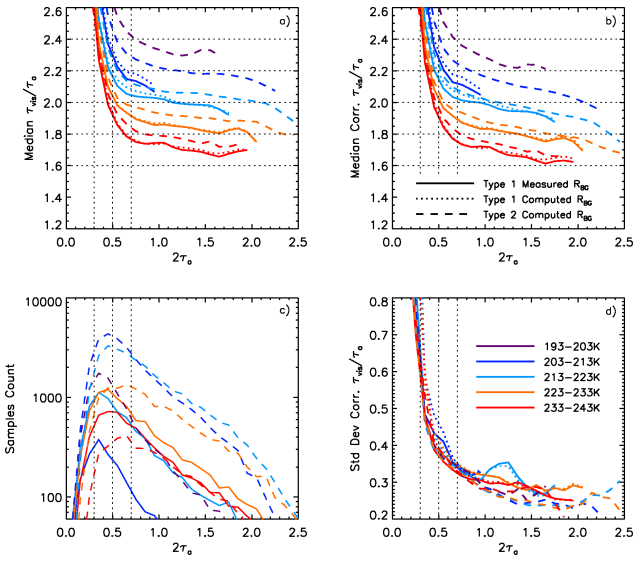

Figure 5. Median τ_{vis}/τ_a ratio against $2\tau_a$ **(a)** from IIR standard products and **(b)** after correction for cloud radiative temperature, **(c)** sample count, and **(d)** τ_{vis}/τ_a ratio standard deviation. Type 1 clouds: measured R_{BG} available and τ_a either from measured R_{BG} (solid) or from computed R_{BG} (dotted); type 2 clouds: no measured R_{BG} available and R_{BG} from computations (dashed). Colors are for temperature at centroid altitude T_c in 193–203 K (purple), 203–213 K (navy blue), 213–223 K (light blue), 223–233 K (orange), and 233–243 K (red). The vertical dotted lines highlight the results for $2\tau_a$ between 0.3 and 0.7 (see text). Data set: single-layered cirrus randomly oriented ice with high confidence, base temperature $< -20\,^{\circ}$C, over ocean, 25° S–25° N, 2008.

4.2 Systematic errors: CALIOP

As seen in Sect. 2.1, CALIOP optical depth is retrieved using the constrained technique only when the estimated relative uncertainty in the derived lidar ratio is less than 40 %, and this relative uncertainty increases rapidly for small optical depths. Because the signal is noisy, optical depth distributions derived from constrained retrievals are increasingly truncated as actual optical depth decreases, because a larger fraction of these small optical depths does not satisfy the estimated relative uncertainty requirement and thus is excluded from the sample data set. This leads to an increasing high bias in constrained optical depths τ_{vis} as optical depth decreases, which explains the sharp increase of the τ_{vis}/τ_a ratio seen in Fig. 5 as $2\tau_a$ decreases.

In order to confirm this interpretation, the analysis is now applied to all the layers for which an apparent two-way transmittance could be measured, including those that do not satisfy the conditions required for the constrained technique, as introduced in Sect. 2.1. An extended set of CALIOP optical depth measurements is thus obtained from Eqs. (1) and (2), still limited to nighttime data, and is compared to IIR τ_a retrievals. Median τ_{vis}/τ_a ratios for the standard constrained retrievals (thin lines) and for the extended optical depth data

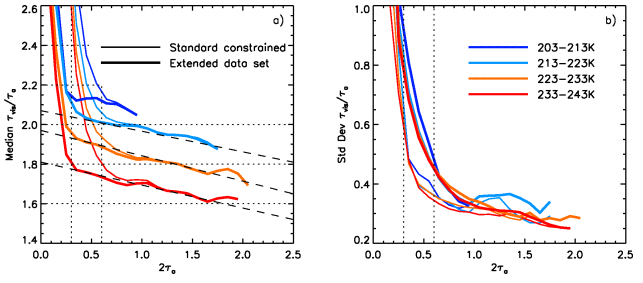

Figure 6. (a) Median τ_{vis}/τ_a ratio and **(b)** standard deviation from standard CALIOP constrained retrievals (thin lines) and from extended CALIOP optical depth measurements (thick lines) for type 1 clouds retrieved from measured R_{BG} after correction for cloud radiative temperature. The vertical dotted lines highlight the differences for $2\tau_a$ between 0.3 and 0.6 (see text). Same data set and color code as in Fig. 5.

set (thick lines) are shown in Fig. 6a for type 1 clouds only for more clarity, after correction of IIR τ_a for the cloud radiative temperature, and again for several ranges in temperature T_c. Associated standard deviations are plotted in Fig. 6b. For the extended data set (thick lines), the τ_{vis}/τ_a ratios now increase steadily from the largest optical depths down to $2\tau_a = 0.3$, suggesting that the extended CALIOP optical depth distributions are not as biased for this data set. A sharp increase of the τ_{vis}/τ_a ratio is still seen for $2\tau_a$ smaller than 0.3, as this ratio of two small numbers becomes more sensitive to small residual biases. In addition, the τ_{vis} distributions are still truncated, because non-physical negative optical depths due to random noise are discarded from the analysis. Standard deviations of the τ_{vis}/τ_a ratios are larger for the extended than for the standard constrained data set, suggesting larger random errors because CALIOP distributions are not as severely truncated in the former case. Implications are threefold. First, this confirms that IIR τ_a retrievals are not biased by unidentified issues. Secondly, this highlights a systematic bias in all CALIOP standard constrained retrievals (thin lines) for optical depths smaller than about 0.6, which is of the order of +50 % at $2\tau_a = 0.3$. This translates into similar relative biases in the retrieved lidar ratios, which is of importance when cirrus lidar ratios derived from constrained retrievals are used to evaluate the default lidar ratio used in unconstrained retrievals (Garnier et al., 2012b). Finally, this shows that the constrained technique could be improved, in the mean, by relaxing the threshold in the relative lidar ratio uncertainties used in version 3 of the CALIOP algorithm, notwithstanding the large dispersion.

4.3 Retrieved τ_{vis}/τ_a ratios

In the following, the retrieved median τ_{vis}/τ_a ratios are discussed. Results obtained after τ_a is corrected for cloud radiative temperature are considered. As seen in Figs. 5 and 6, the ratios are found to increase by about 10 % as the temperature T_c decreases by 10 K. The ratios derived from type 1 clouds are found between 1.6 at 233–243 K and 2.1 at 203–213 K, with a standard deviation of the order of 0.3 at $2\tau_a$ larger than 1. For type 2 clouds, the ratios are larger by 2 to 5 %, which could be partly explained by possible biases on IIR τ_a retrievals. Nevertheless, as both type 1 and type 2 clouds exhibit the same behavior with respect to temperature, they will be combined in the following analyses. To reduce the impact of biases, subsequent analyses are limited to cases for which $2\tau_a$ is larger than 0.3. Also, CALIOP extended optical depth retrievals are chosen to avoid biases in CALIOP standard constrained retrievals. For a given temperature, the ratios decrease by about 10 % from $2\tau_a = 0.3$ to $2\tau_a = 2$, as seen in Fig. 6a. This may be due partly to an increasing contribution of multiple scattering in τ_a, yet expected to not increase by more than 2 % according to simulations performed on numerous crystal habits.

The clear dependence of τ_{vis}/τ_a on temperature T_c is interesting. According to the simulations shown in Fig. 2 for the 12.05 µm IIR channel, for effective diameters larger than 10–15 µm, the ratios are expected to increase as the effective diameter increases, with little sensitivity to effective diameters larger than 100 µm. Thus, the increase of the observed τ_{vis}/τ_a with decreasing T_c could conceivably be caused by larger crystals, but this is in contradiction with the fact that mean crystal sizes and effective diameters are known to be generally decreasing with decreasing temperature for clouds of moderate optical depth smaller than 2.5 as considered in this study (see for example Heymsfield et al., 2014). Observations could also be explained by ice crystals effective diameters decreasing from 10–15 µm at $T_c = 240$ K down to 5 µm at $T_c = 200$ K, but this is very unlikely according to recent analyses of in situ observations (Heymsfield et al., 2014, and references herein). To go further in the discussion, ice crystal effective diameters retrieved from IIR measurements in the three available channels are investigated. The fundamental parameters are the so-called microphysical indices $\beta_{12/10}$ and $\beta_{12/08}$, defined as the ratios of τ_a from channel 12.05 µm to the absorption optical depths retrieved at 10.6 and at 08.65 µm, respectively (Garnier et al., 2013). These indices can be converted into an effective diameter through lookup tables, as illustrated in Fig. 7a, which shows the theoretical microphysical indices $\beta_{12/10}$ (solid lines) and $\beta_{12/08}$ (dashed lines) derived for hexagonal solid columns (blue) and aggregates (red) for $\tau_a = 0.25$. The effective diameter is derived from the crystal model for which the relationship between $\beta_{12/10}$ and $\beta_{12/08}$ agrees the best with the observations. More details about the IIR microphysical algorithm can be found in Garnier et al. (2013). Figure 7b shows the cumulative probability density function of the derived effective diameter D_e. As discussed earlier, the analysis is applied to clouds exhibiting an optical depth $2\tau_a$ larger than 0.3, which allows minimizing possible biases in IIR retrievals at small optical depth. Still, as the IIR microphysical retrievals are the most robust for type 1 clouds with R_{BG} derived from ob-

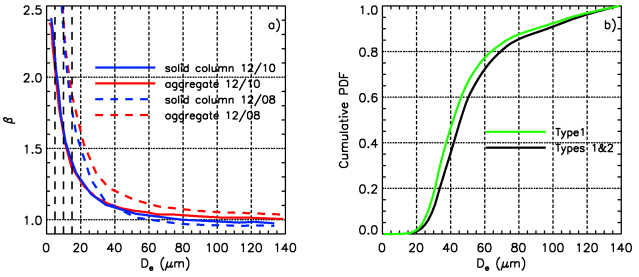

Figure 7. (a) Theoretical microphysical indices $\beta_{12/10}$ (solid lines) and $\beta_{12/08}$ (dashed lines) against effective diameter D_e for a cloud composed of hexagonal solid columns (blue) and of aggregates (red), with $\tau_a = 0.25$. The vertical dashed lines highlight the large sensitivity to D_e smaller than 15 µm (see text). **(b)** Cumulative probability density function of D_e retrieved from IIR microphysical indices for type 1 clouds (green, measured R_{BG}) and by combining type 1 and type 2 clouds (black). Data set: single-layered cirrus randomly oriented ice with high confidence, base temperature $< -20\,°C$, extended CALIOP optical depth measurements, $2\tau_a > 0.3$, over ocean, 2008.

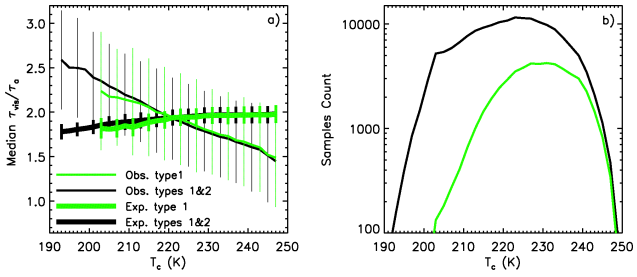

Figure 8. (a) Median observed (thin lines) and expected (thick lines) τ_{vis}/τ_a ratio ± standard deviation and **(b)** associated samples count against temperature T_c for type 1 clouds (green, measured R_{BG}) and combined type 1 and type 2 clouds (black). Same data set as in Fig. 7b.

servations as described in Garnier et al. (2013), the results are shown for type 1 clouds (green) only and by combining type 1 and type 2 clouds (black) in order to assess the impact of possible biases in the latter case. For both configurations, only 0.3 % of the retrieved diameters are smaller than 15 µm, which confirms that the observed behavior of the τ_{vis}/τ_a ratios with respect to T_c cannot be explained by very small crystal sizes, especially because IIR retrievals are the most sensitive to small sizes, as evidenced in Fig. 7a.

IIR microphysical retrievals are representative of the small mode of the particle size distribution (Mitchell et al., 2010). Nonetheless, they indicate that IIR absorption optical depth is sensitive to the presence of ice crystals exhibiting these ranges in effective diameter, and the expected τ_{vis}/τ_a ratio can be estimated from the simulations shown in Fig. 2. The median expected ratios are plotted in Fig. 8a against the centroid temperature T_c (thick lines), together with the median observed ratios (thin lines) to facilitate the discussion. The green curves are for type 1 clouds whereas the black curves show the results obtained by combining type 1 and type 2 clouds. As the black and green curves are very close in the overlapping region, the analysis is conducted by combining all clouds to take advantage of the larger number of samples, especially at the coldest temperatures (Fig. 8b). The expected τ_{vis}/τ_a ratio (thick lines) steadily increases from 1.8 ± 0.1 at $T_c = 195$ K up to 1.95 ± 0.1 at T_c larger than 230 K. This result is driven by the fact that effective diameters are found increasing as temperature increases from 195 up to 230 K, and with a decreasing occurrence of retrieved hexagonal solid columns, as will be shown in Sect. 4.5.

There is an obvious disagreement between observed and expected variations with temperature of the τ_{vis}/τ_a ratios, which needs to be explained. The accuracy of the theoretical simulations is difficult to assess, but it is unlikely that they do not correctly reproduce the general behavior with respect to effective diameter. The expected τ_{vis}/τ_a ratios are weakly sensitive to the microphysical properties, so that the overall disagreement between observed and expected ratios is unlikely to be attributable to errors in IIR microphysical retrievals. However, even though CALIOP retrievals are robust because they are directly derived from the measured cloud layer two-way transmittance, the retrieved quantity is the apparent optical depth, which can be converted to the single-scattering optical depth only after applying a correction for the effect of multiple scattering. After rewriting Eq. (2) as

$$\tau_{apparent} = \eta \cdot \tau_{vis} = \eta_T \cdot \tau_{vis,T}, \quad (14)$$

where η_T is the "true" multiple scattering correction factor and $\tau_{vis,T}$ is the "true" single-scattering visible optical depth, it can be seen that variations of τ_{vis}/τ_a could be accounted for by a correction factor η_T, which increases as T_c decreases. This tentative explanation is investigated in the following section.

4.4 CALIOP multiple scattering factor

Following the approach introduced by Platt (1973), the "bulk" multiple scattering factors η_T, derived by reconciling the observed and the expected ratios of visible optical depth to infrared absorption optical depth, are now examined. For every cloud sample used to build Fig. 8a, we invoke the relationship given in Eq. (14) to derive

$$\eta_T = \eta \cdot \frac{\left(\tau_{vis}/\tau_a\right)_{observed}}{\left(\tau_{vis}/\tau_a\right)_{expected}}. \quad (15)$$

The 2-D histogram of η_T (y axis) and T_c (x axis) is shown in Fig. 9a for the same data set as in Fig. 8 and by combining type 1 and type 2 clouds. The mean multiple scattering factor is found to be decreasing from $\eta_T = 0.8$ at $T_c = 200$ K to $\eta_T = 0.6$ at 220 K and then more slowly to $\eta_T = 0.5$ at 240 K, which is the lower limit if scattering is only due to diffraction

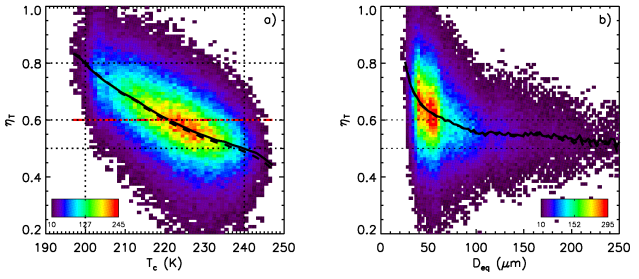

Figure 9. Two-dimensional histogram of multiple scattering factor η_T and **(a)** temperature T_c and **(b)** equivalent diameter D_{eq}. The color code is the number of samples. The median and mean values against T_c are the black solid and dashed lines, respectively. In Fig. 9a, the horizontal red dotted dashed line shows the mean value of η_T overall (0.601). The dotted lines indicate values discussed in the text. Same data set as in Fig. 8, all clouds combined.

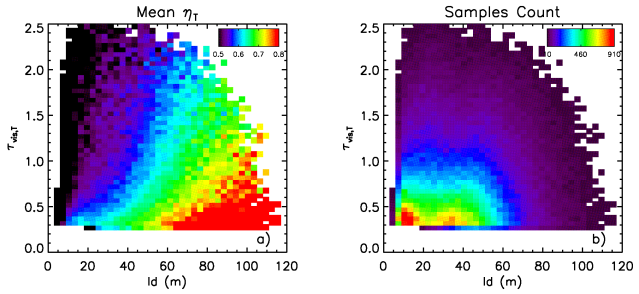

Figure 10. (a) Mean value of the multiple scattering factor η_T as a function of visible optical depth ($\tau_{vis,T}$) and estimated lateral displacement (ld); **(b)** associated number of samples. Same data set as in Fig. 9.

(Hogan, 2008). The overall mean value of η_T is 0.601, which is encouraging, since this is essentially identical to the constant value $\eta = 0.6$ used in the version 3 CALIOP operational algorithm. The results shown in Fig. 9 are for the 12 months of 2008. The same analysis has been applied during 2010 and 2012, and very similar results within a few percents over the whole range of temperature are obtained (not shown), with overall mean values of η_T equal to 0.604 and 0.602, respectively. Lamquin et al. (2008) also found larger values of η_T at temperatures colder than 210 K than at 230–240 K. Josset et al. (2012) reported a mean value $\eta_T = 0.61 \pm 0.15$ for mid-layer temperatures colder than 233 K but by considering $(\tau_{vis} / \tau_a)_{expected}$ from Eq. (15) about 15 % larger than established from this study.

Variations of the multiple scattering factor reflect changes in the probability that a scattered photon will stay within the field of view and subsequently contribute to the measured signal. This probability becomes smaller as the lateral displacement of the photon in the clear region below the cloud increases and possibly exceeds the receiver footprint. The lateral displacement increases with the diffraction angle θ, which is inversely proportional to the ice crystal equivalent diameter D_{eq}, defined as the diameter of a sphere of equivalent volume (Nicolas et al., 1997; Comstock and Sassen, 2001). For further evaluation, the 2-D histogram of η_T and equivalent D_{eq} derived from the IIR microphysical algorithm is shown in Fig. 9b. It is seen that, as expected, the mean value of η_T progressively decreases as D_{eq} increases or as the diffraction angle θ decreases. As the IIR effective diameter is sensitive to the small mode of the size distribution, it is a priori underestimated for many of these clouds, so that only qualitative conclusions can be drawn. Finally, the relation between η_T and a simplified estimate of the lateral displacement resulting from forward diffraction only is examined. By taking the centroid altitude Z_c as the "bulk" cloud altitude, the distance between the diffracting ice crystals and the region where the two-way transmittance is measured is the difference between Z_c and the altitude Z_b taken 2 km below the cloud base altitude. Thus, the lateral geometric displacement (ld) is roughly estimated as

$$\mathrm{ld} = \theta \cdot (Z_c - Z_b) = \frac{1.22\lambda}{D_{eq}} \cdot (Z_c - Z_b)\,. \quad (16)$$

Figure 10a shows the mean value of the multiple scattering factor η_T as a function of the "true" visible optical depth $\tau_{vis,T}$ derived from Eq. (14) and of the estimated lateral displacement. The corresponding number of samples is shown in Fig. 10b. For most samples, optical depth is smaller than 1 and the estimated ld is found to be smaller than 60 m. For comparison, the radius of the CALIOP receiver footprint is about 50 m and the radius of the laser footprint is about 42 m (Hunt et al., 2009). The mean value of η_T is found to be increasing toward the single-scattering limit ($\eta_T = 1$) as the estimated value of ld increases (Fig. 10a) and increasing less rapidly as optical depth increases. It is recognized that ld is a crude estimate based on simplified geometric considerations and scattering due to diffraction only, and a quantified discussion would be hazardous. Nonetheless, these qualitative results indicate that the "bulk" multiple scattering factors η_T derived by reconciling observed and expected τ_{vis} / τ_a ratios at cloud layer scale are a real measurement of the result of the complex journey of the photons within and below the layer due to diffraction and scattering.

4.5 Discussion: implications for CALIOP retrievals

Several parameters related to ice crystal microphysics are retrieved from the CALIPSO mission. Lidar ratios derived from measurements of the two-way transmittance provide insights into ice crystals scattering phase function at 180°, and depolarization ratios at 532 nm are an indicator of ice crystal shape ratios (Noël et al., 2002). These measured parameters, available at global scale, have been compared with simulations for numerous ice crystal models (Baum et al., 2011). The depolarization ratio of semi-transparent cirrus clouds observed by CALIOP is not expected to be signif-

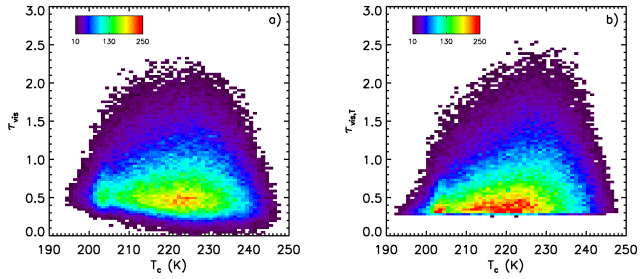

Figure 11. Two-dimensional histogram of **(a)** τ_{vis} ($\eta = 0.6$) and **(b)** $\tau_{vis,T}$ (η_T from this study), and centroid temperature T_c. The color code is the number of samples. Same data set as in Fig. 9.

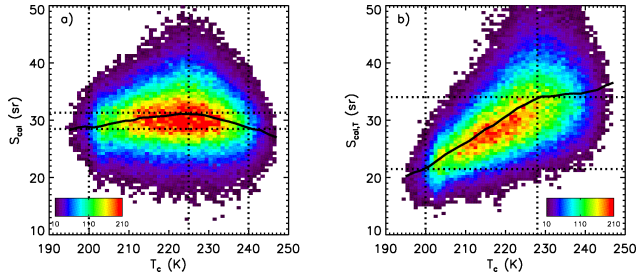

Figure 12. Two-dimensional histogram of lidar ratio **(a)** S_{cal} ($\eta = 0.6$) and **(b)** $S_{cal,T}$ (η_T from this study) and centroid temperature T_c. The color code is the number of samples. The black solid line is the median value. The dotted lines indicate minimum and maximum values and associated temperatures (see text). Same data set as in Fig. 9.

icantly impacted by multiple scattering (Reichardt and Reichardt, 2003). However, the derived lidar ratio is inversely proportional to the multiple scattering factor (see Eq. 5).

The changes in optical depth and lidar ratio resulting from using η_T as derived above, instead of $\eta = 0.6$ as used in the standard retrieval, are now examined.

4.5.1 Optical depth

The multiple scattering factor has been found to vary between $\eta_T = 0.8$ and $\eta_T = 0.5$ as temperature increases and to be equal to 0.6 on average. In this case, the CALIOP optical depth retrieved by using a constant value $\eta = 0.6$ is overestimated by 30 % on average at the coldest temperatures and underestimated by 15 % on average at the warmest ones. The resulting changes in optical depth histograms are shown in Fig. 11, which compares the 2-D histograms of τ_{vis} ($\eta = 0.6$, Fig. 11a) and $\tau_{vis,T}$ derived from Eq. (14) (η_T, Fig. 11b) and centroid temperature, T_c. Note that in Fig.11b, $\tau_{vis,T}$ is mostly larger than 0.3, because the analysis is conducted for $2\tau_a$ larger than 0.3. $\tau_{vis,T}$ exhibits a general increase with increasing temperature (Fig. 11b), which is not seen in τ_{vis} (Fig. 11a). This implies that on average, the extinction coefficients derived from CALIOP using η_T would increase more rapidly with temperature than those retrieved using $\eta = 0.6$. This change would also be reflected in the ice water content estimates reported in the CALIOP data products, because ice water content is inferred from a parameterization based on extinction coefficients (Heymsfield et al., 2005, 2014).

4.5.2 Parameters related to microphysics

Lidar ratios can be derived using Eqs. (3) and (5) with constant or variable multiple scattering factors. Figure 12 compares the 2-D histograms of S_{cal} ($\eta = 0.6$, Fig. 12a) and $S_{cal,T}$ (η_T, Fig. 12b) and centroid temperature, T_c. When η is taken constant, the median lidar ratio S_{cal} is found to be weakly varying with temperature, with a maximum $S_{cal} = 31$ sr at $T_c = 225$ K and minima at $T_c = 200$ and 240 K that are smaller by only 10 % ($S_{cal} = 28$ sr). Because η is taken constant, we can conclude that the apparent lidar ratio S^* is likewise only weakly varying with temperature. When the multiple scattering factor is taken from this study (η_T), the temperature dependence is increased, as the median lidar ratio $S_{cal,T}$ is found to increase by about 50 % from $S_{cal,T} = 21$ sr at $T_c = 200$ K up to $S_{cal,T} = 34$ sr at $T_c = 228$ K and to be roughly constant for T_c warmer than 228 K These findings are qualitatively consistent with airborne observations over the Pacific Ocean as reported by Yorks et al. (2011).

Cirrus lidar ratio and depolarization are both expected to vary somewhat with crystal habit. Distributions of the integrated volume (blue) and particulate (red) depolarization ratios reported in the CALIOP products are shown in Fig. 13a. The particulate depolarization ratio is derived from the standard extinction solutions and thus according to this analysis should be expected to change slightly. Nevertheless, the temperature-dependent behavior of the particulate depolarization ratio is similar to the volume depolarization ratio, which indicates that contributions from molecular scattering is weak and therefore that the current particulate depolarization ratio provides sufficient accuracy for this discussion. As for the lidar ratio $S_{cal,T}$, the depolarization ratio is found to be essentially constant at T_c larger than 228 K, and it is found to be increasing as T_c gets colder. This behavior is consistent with observations reported in Sassen and Benson (2001) based on profiles from ground-based ruby lidar located in Salt Lake City, Utah. Furthermore, as seen in Fig. 13b, IIR retrievals suggest a decrease in the occurrence of hexagonal solid columns as T_c increases up to the same limit $T_c = 228$ K, with no temperature dependence at warmer temperatures. Keeping in mind that this analysis is conducted for clouds dominated by randomly oriented ice crystals, both Fig. 13a and b suggest a progressive transition from solid columns-like crystals having large aspect shape ratios and depolarization ratios (Noël et al., 2002) at colder temperatures to more compact and less depolarizing crystals as temperatures increase. The inferred changes of crystal habit with temperature are in good agreement with in situ observations (Bailey and Hallett, 2009). Relationships between lidar ra-

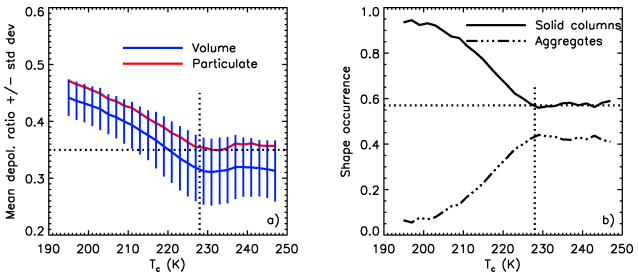

Figure 13. (a) Mean ± standard deviation volume (blue) and particulate (red) depolarization ratio against T_c; **(b)** IIR retrieved shape occurrence against T_c. The dotted lines indicate variations with T_c discussed in the text. Same data set as in Fig. 9.

tios and depolarization ratios have been reported by numerous authors (e. g. Chen et al., 2002; Reichardt et al., 2002; Yorks et al., 2011), and a degree of correlation is expected. Overall, these observations show an apparent consistency between several independently retrieved parameters in terms of variations with layer centroid temperature. The improved correlation between depolarization ratio and lidar ratio when the latter is derived using η_T rather than by assuming a constant value is noticeable and deemed another indication of the overall consistency of our analyses.

5 Conclusions

Infrared absorption optical depths (τ_a) retrieved from IIR observations of cirrus clouds at 12.05 µm are compared to visible extinction optical depths (τ_{vis}) derived from CALIOP observations of the same cloud when direct measurements of the apparent two-way transmittance are available. IIR absorption optical depths are derived for suitable scenes selected by taking advantage of the vertical information available from collocated CALIOP observations. In this paper, we focus on single-layered cirrus clouds over ocean, composed of randomly oriented ice according to CALIOP ice–water classification (high confidence) and with base temperatures colder than −20 °C.

The retrieved τ_{vis}/τ_a ratios exhibit an unexpected quasi-linear dependence with temperature at layer centroid altitude T_c. The observed values increase by about 10 % for each 10 K decrease in temperature over a range from $T_c = 240$ K down to $T_c = 200$ K. This behavior is not consistent with theoretical expectations inferred from simulations and IIR microphysical retrievals of ice crystal effective diameter D_e and most probable crystal shape. The suggested explanation is a temperature-dependent multiple scattering factor η_T, which is assumed constant and equal to 0.6 in CALIOP version 3 optical depth retrievals.

A "bulk" multiple scattering factor is derived by reconciling the retrieved and expected τ_{vis}/τ_a ratios after a detailed analysis of possible biases and after applying corrections, whenever relevant. For IIR, it is shown that the cloud radiative temperature can be derived a posteriori from CALIOP cloud extinction profiles. IIR standard version 3 absorption optical depths are corrected a posteriori and are augmented by 1 to 17 % with corrections that increase with geometric thickness and optical depth. Biases resulting from the background radiances computed using the radiative transfer model and GEOS 5 ancillary data are also evaluated by comparing retrievals for which τ_a is from computed background radiances (type 2 clouds) with more accurate retrievals for which the background radiance could be measured in neighboring pixels (type 1 clouds). After correction for the cloud radiative temperature, the τ_{vis}/τ_a ratios for type 1 and type 2 clouds are found in satisfactory agreement. The multiple scattering factor is therefore derived by combining both types of clouds, which ensures a significant number of samples between 200 and 240 K. For CALIOP, selection biases in standard version 3 constrained retrievals are seen for visible optical depths smaller than about 0.6. When using only those optical depths originally accepted by the constrained retrieval algorithm, optical depth selection biases are seen to increase as optical depth decreases. For optical depths of 0.3, these biases introduce an overestimate of ∼ 50 %. For this analysis, all the layers for which an apparent two-way transmittance could be measured are considered, as using this extended data set substantially improves the τ_{vis}/τ_a ratios at small optical depths while at the same time substantially increasing the number of layers included in the study. However, because biases are still evidenced at $2\tau_a$ smaller than 0.3, the multiple scattering factor is only estimated for $2\tau_a$ larger than this limit.

The bulk multiple scattering factor is found to decrease from $\eta_T = 0.8$ at $T_c = 200$ K to $\eta_T = 0.5$ at $T_c = 240$ K and to be equal to 0.6 on average. The temperature dependence of η_T retrieved from this study appears plausible according to simplified estimates of key parameters driving the multiple scattering factor. The next step in the assessment would be to perform detailed simulations in order to improve the accuracy of the current results. These findings, if confirmed, would imply that CALIOP optical depth and extinction coefficients from constrained retrievals are on average overestimated by about 30 % at $T_c = 200$ K and underestimated by about 15 % at $T_c = 240$ K for the data set selected in this study. This statement would need to be confirmed through comparisons with retrievals from other instruments. The apparent consistency between several independently retrieved parameters related to microphysics, namely the integrated depolarization ratio, the ice crystal shape occurrence derived from the IIR, and the lidar ratio is reinforced when the latter is derived from η_T rather than by assuming a constant value. The increased correlation between lidar ratio and depolarization ratio is considered to be further evidence that the η_T parameterization more accurately reflects the underlying microphysics of cirrus clouds. These results could contribute to a better characterization of optically thin cirrus clouds at

night over ocean, with subsequent opportunities for improved understanding of possible formation mechanisms.

This paper illustrates the added value of synergetic analyses of perfectly collocated retrievals from the IIR passive radiometer and the CALIOP active lidar. Understanding and estimating biases, even for a limited data set, allows refining uncertainty estimates and improving the consistency of the retrievals and provides guidance for the development of future versions of the products. Continuous assessment and improvement of the CALIPSO data record, now spanning 9 years in both the visible and the thermal infrared spectral domains, are of importance for a better understanding of the radiative impact of cirrus clouds at global scale.

Acknowledgements. The authors thank Steve Platnick and Bob Holz for many fruitful discussions about active and passive remote sensing retrievals and thank Ping Yang for providing the ice crystal optical properties used in our simulation studies. The authors are grateful to the ICARE data center in France for their help with the development of the IIR Level 2 algorithm. CALIPSO products are publicly available at the Atmospheric Science Data Center of the NASA Langley Research Center and at ICARE data center. The authors are thankful to Patricia Lucker for her support, to CNES, and to CNRS (Centre National de la Recherche Scientifique).

Edited by: V. Amiridis

References

Bailey, M. and Hallett, J.: A comprehensive habit diagram for atmospheric ice crystals: confirmation from the laboratory, AIRS II, and other field studies, J. Atmos. Sci., 66, 2888–2899, 2009.

Baum, B. A., Yang, P., Heymsfield, A. J., Schmitt, C. G., Xie, Y., Bansemer A., Hu, Y.-X., and Zhang, Z.: Improvements in shortwave bulk scattering and absorption models for the remote sensing of ice clouds, J. Appl. Meteorol. Clim., 50, 1037–1056, doi:10.1175/2010JAMC2608.1, 2011.

Berry, E. and Mace, G. G.: Cloud properties and radiative effects of the Asian summer monsoon derived from A-Train data, J. Geophys. Res., 119, 9492–9508, doi:10.1002/2014JD021458, 2014.

Chen, W. N., Chiang, C. W., and Nee, J. B.: Lidar ratio and depolarization ratio for cirrus clouds, Appl. Optics, 41, 6470–6476, doi:10.1364/AO.41.006470, 2002.

Chepfer, H., Pelon, J., Brogniez, G., Flamant, C., Trouillet, V., and Flamant, P. H.: Impact of cirrus cloud ice crystal shape and size on multiple scattering effects: Application to spaceborne and airborne backscatter lidar measurements during LITE mission and E-LITE campaign, Geophys. Res. Lett., 26, 2203–2206, 1999.

Comstock, J. and Sassen, K.: Retrieval of cirrus cloud radiative and backscattering properties using combined lidar and infrared radiometer (LIRAD) measurements, J. Atmos. Ocean. Tech., 18, 1658–1673, 2001.

Corlay, G., Arnolfo, M.-C., Bret-Dibat, T., Lifermann, A., and Pelon, J.: The infrared imaging radiometer for PICASSO-CENA, available at: http://smsc.cnes.fr/CALIPSO/IIR_ICSO00_S2-06.pdf (last access: 23 February 2015), 2000.

Del Guasta, M.: Errors in the retrieval of thin-cloud optical parameters obtained with a two-boundary algorithm, Appl. Optics, 37, 5522–5540, 1998.

Dubuisson, P., Giraud, V., Chomette, O., Chepfer, H., and Pelon, J.: Fast radiative transfer modeling for infrared imaging radiometry, J. Quant. Spectrosc. Ra., 95, 201–220, 2005.

Dubuisson, P., Giraud, V., Pelon, J., Cadet, B., and Yang, P.: Sensitivity of thermal infrared radiation at the top of the atmosphere and the surface to ice cloud microphysics. J. Appl. Meteor. Clim., 47, 2545–2560, 2008.

Eloranta, E. W.: A practical model for the calculation of multiply scattered lidar returns. Appl. Optics, 37, 2464–2472, 1998.

Elouragini, S. and Flamant, P. H.: Iterative method to determine an averaged backscatter-to-extinction ratio in cirrus clouds, Appl. Optics, 35, 1512–1518, 1996.

Garnier A., Pelon, J., Dubuisson, P., Faivre, M., Chomette, O., Pascal, N., and Kratz, D. P.:Retrieval of cloud properties using CALIPSO Imaging Infrared Radiometer. Part I: effective emissivity and optical depth, J. Appl. Meteorol. Clim., 51, 1407–1425, doi:10.1175/JAMC-D-11-0220.1, 2012a.

Garnier, A., Vaughan, M. A., Dubuisson, P., Josset, D., Pelon, J., and Winker, D. M.: Multi-sensor cirrus optical depth estimates from CALIOP, in: Reviewed and Revised Papers Presented at the 26th International Laser Radar Conference, Porto Heli, Greece, 25–29 June 2012, 691–694, 2012b.

Garnier, A., Pelon, J., Dubuisson, P.,Yang, P., Faivre, M., Chomette, O., Pascal, N., Lucker, P., and Murray, T.: Retrieval of cloud properties using CALIPSO Imaging Infrared Radiometer. Part II: effective diameter and ice water path, J. Appl. Meteorol. Clim., 52, 2582–2599, doi:10.1175/JAMC-D-12-0328.1, 2013.

Heymsfield, A., Winker, D., and van Zadelhoff, G.-J.: Extinction-ice water content-effective radius algorithms for CALIPSO, Geophys. Res. Lett., 32, L10807, doi:10.1029/2005GL022742, 2005.

Heymsfield, A., Winker, D., Avery, M., Vaughan, M., Diskin, G., Deng, M., Mitev, V., and Matthey, R.: Relationships between ice water content and volume extinction coefficient from in situ observations for temperatures from 0° to −86 °C: Implications for spaceborne lidar retrievals, J. Appl. Meteorol. Clim., 53, 479–505, doi:10.1175/JAMC-D-13-087.1, 2014.

Hogan, R. J.: Fast lidar and radar multi-scattering models. part I: Small-angle scattering using the photon variance-covariance method, J. Atmos. Sci., 65, 3621–3635, 2008.

Hu, Y., Vaughan, M., Liu, Z., Powell, K., and Rodier, S.: Retrieving optical depths and lidar ratios for transparent layers above opaque water clouds from CALIPSO lidar measurements, IEEE Geosci. Remote, 4, 523–526, doi:10.1109/LGRS.2007.901085, 2007.

Hu, Y., Winker, D., Vaughan, M., Lin, B., Omar, A., Trepte, C., Flittner, D., Yang, P., Nasiri, S. L., Baum, B., Holz, R., Sun, W., Liu, Z., Wang, Z., Young, S., Stamnes, K., Huang, J., and Kuehn, R.: CALIPSO/CALIOP cloud phase discrimination algorithm, J. Atmos. Ocean. Tech., 26, 2293–2309, doi:10.1175/2009JTECHA1280.1, 2009.

Hu, Y., Rodier, S., Xu, K., Sun, W., Huang, J., Lin, B., Zhai, P., and Josset, D.: Occurrence, liquid water content, and fraction of supercooled water clouds from combined CALIOP/IIR/MODIS measurements, J. Geophys. Res., 115, D00H34, doi:10.1029/2009JD012384, 2010.

Hunt, W. H., Winker, D. M., Vaughan, M. A., Powell, K. A., Lucker, P. L., and Weimer, C.: CALIPSO lidar description and performance assessment, J. Atmos. Ocean. Tech., 26, 1214–1228, doi:10.1175/2009JTECHA1223.1, 2009.

Josset, D., Pelon, J., Garnier, A., Hu, Y.-X., Vaughan, M., Zhai, P., Kuehn, R., and Lucker, P.: Cirrus optical depth and lidar ratio retrieval from combined CALIPSO-CloudSat observations using ocean surface echo, J. Geophys. Res., 117, D05207, doi:10.1029/2011JD016959, 2012.

Lamquin, N., Stubenrauch, C. J., and Pelon, J.: Upper tropospheric humidity and cirrus geometrical and optical thickness: relationships inferred from one year of collocated AIRS and CALIPSO data, J. Geophys. Res., 113, D00A08, doi:10.1029/2008JD010012, 2008.

Liu, Z., Vaughan, M. A., Winker, D. M., Kittaka, C., Getzewich, B. J., Kuehn, R. E., Omar, A., Powell, K. A., Trepte, C. R., and Hostetler, C. A.: The CALIPSO lidar cloud and aerosol discrimination: version 2 algorithm and initial assessment of performance, J. Atmos. Ocean. Tech., 26, 1198–1213, 2009.

Mitchell, D. L.: Effective diameter in radiation transfer: general definition, applications, and limitations, J. Atmos. Sci., 59, 2330–2346, 2002.

Mitchell, D. L., d'Entremont, R. P., and Lawson, R. P.: Inferring cirrus size distributions through satellite remote sensing and microphysical databases, J. Atmos. Sci., 67, 1106–1125, doi:10.1175/2009JAS3150.1, 2010.

Nicolas, F., Bissonnette, L. R., and Flamant, P. H.: Lidar effective multiple-scattering coefficients in cirrus clouds, Appl. Optics, 36, 3458–3468, 1997.

Noël, V., Chepfer, H., Ledanois, G., Delaval, A., and Flamant, P. H.: Classification of particle shape ratios in cirrus clouds based on the lidar depolarization ratio, Appl. Optics, 41, 4245–4257, 2002.

Pitts, M. C., Thomason, L. W., Hu, Y., and Winker, D. M.: An assessment of the on-orbit performance of the CALIPSO Wide Field Camera, in: Remote Sensing of Clouds and the Atmosphere XII, SPIE proceedings, Vol. 6745, edited by: Comeron, A., Schäfer, K., Slusser, J. R., Picard, R. H., and Amodeo, A., International Society for Optical Engineering, Florence, Italy, 67450K, doi:10.1117/12.737377, 2007.

Platt, C. M. R.: Lidar and radiometric observations of cirrus clouds, J. Atmos. Sci., 30, 1191–1204, 1973.

Platt, C. M. R. and Gambling, D. J.: Emissivity of high layer clouds by combined lidar and radiometric techniques, Q.. J. Roy. Meteor. Soc., 97, 322–325, 1971.

Platt, C. M. R., Young, S. A., Austin, R. T., Patterson, G. R., Mitchell, D. L., and Miller, S. D.: LIRAD observations of tropical cirrus clouds in MCTEX. Part I: Optical properties and detection of small particles in cold cirrus, J. Atmos. Sci, 59, 3145–3162, 2002.

Powell, K., Vaughan, M. , Winker, D., Lee, K.-P., Pitts, M., Trepte, C., Detweiler, P., Hunt, W., Lambeth, J., Lucker, P., Murray, T., Hagolle, O., Lifermann, A., Faivre, M., Garnier, A., and Pelon, J.: CALIPSO data management systems data products catalog, document No. PC-SCI-503, Release 3.6, available at: http://www-calipso.larc.nasa.gov/products/CALIPSO_DPC_Rev3x6.pdf (last access: 23 February 2015), 2013.

Reichardt, S. and Reichardt, J.: Effect of multiple scattering on depolarization measurements with spaceborne lidars, Appl. Optics, 42, 3620–3633, 2003.

Reichardt, J., Reichardt, S., Hess, M., and McGee, T. J.: Correlations among the optical properties of cirrus-cloud particles: Microphysical interpretation, J. Geophys. Res., 107, 4562, doi:10.1029/2002JD002589, 2002.

Rienecker, M. M., Suarez, M. J., Todling, R., Bacmeister, J., Takacs, L., Liu, H.-C., Gu, W., Sienkiewicz, M., Koster, R. D., Gelaro, R., Stajner, I., and Nielsen, J. E.: The GEOS-5 data assimilation system – Documentation of versions 5.0.1, 5.1.0, and 5.2.0, Technical Report Series on Global Modeling and Data Assimilation, 27, NASA/TM-2008-104606,1-118, 2008.

Sassen, K. and Benson, S.: A midlatitude cirrus cloud climatology from the facility for atmospheric remote sensing. Part II: Microphysical properties derived from lidar depolarization, J. Atmos. Sci., 58, 2103–2112, 2001.

Sassen, K., Wang, Z., and Liu, D.: Global distribution of cirrus clouds from CloudSat/Cloud-Aerosol Lidar and Infrared Pathfinder Satellite Observations (CALIPSO) measurements, J. Geophys. Res., 113, D00A12, doi:10.1029/2008JD009972, 2008.

Sourdeval, O., Brogniez, G., Pelon, J., Labonnote, L. C., Dubuisson, P., Parol, F., Josset, D., Garnier, A., Faivre, M., and Minikin, A.: Validation of IIR/CALIPSO level 1 measurements by comparison with collocated airborne observations during CIRCLE-2 and Biscay '08 Campaigns, J. Atmos. Ocean. Tech., 29, 653–667, doi:10.1175/JTECH-D-11-00143.1, 2012.

Vaughan, M. A., Winker, D. M., and Powell, K. A.: CALIOP algorithm theoretical basis document, Part 2: Feature detection and layer properties algorithms, PC-SCI-202.02, NASA Langley Research Center, Hampton, VA 23681, 87 pp., available at: http://www-calipso.larc.nasa.gov/resources/project_documentation.php (last access: 23 February 2015), 2005.

Vaughan, M. A., Powell, K. A., Winker, D. M., Hostetler, C. A., Kuehn, R. E., Hunt, W. H., Getzewich, B. J., Young, S. A., Liu, Z., and McGill, M. J.: Fully automated detection of cloud and aerosol layers in the CALIPSO lidar measurements, J. Atmos. Ocean. Tech., 26, 2034–2050, doi:10.1175/2009JTECHA1228.1, 2009.

Winker, D. M.: Accounting for multiple scattering in retrievals from space lidar, Proc. SPIE Int. Soc. Opt. Eng., 5059, 128–139, 2003.

Winker, D. M., Vaughan, M. A., Omar, A. H., Hu, Y., Powell, K. A., Liu, Z., Hunt, W. H., and Young, S. A.: Overview of the CALIPSO mission and CALIOP data processing algorithms, J. Atmos. Ocean. Tech., 26, 2310–2323, doi:10.1175/2009JTECHA1281.1, 2009.

Winker, D. M., Pelon, J., Coakley Jr., J. A., Ackerman, S. A., Charlson, R. J., Colarco, P. R., Flamant, P., Fu, Q., Hoff, R., Kittaka, C., Kubar, T. L., LeTreut, H., McCormick, M. P., Megie, G., Poole, L., Powell, K., Trepte, C., Vaughan, M. A., and Wielicki, B. A.: The CALIPSO mission: a global 3D view of aerosols and clouds, B. Am. Meteorol. Soc., 91, 1211–1229, 2010.

Yang, P., Wei., H., Huang, H. L., Baum, B. A., Hu, Y. X., Kattawar, G. W., Mishchenko, M. I., and Fu, Q.: Scattering and absorption property database for non-spherical ice particles in the near- through far-infrared spectral region, Appl. Optics, 44, 5512–5523, 2005.

Yorks, J. E., Hlavka, D. L., Hart, W. D., and McGill, M. J.: Statistics of cloud optical properties from airborne lidar measurements, J. Atmos. Ocean. Tech., 28, 869–883, doi:10.1175/2011JTECHA1507.1, 2011.

Young, S. A.: Analysis of lidar backscatter profiles in optically thin clouds, Appl. Optics, 34, 7019–7031, doi:10.1364/AO.34.007019, 1995.

Young, S. A. and Vaughan, M. A.: The retrieval of profiles of particulate extinction from Cloud-Aerosol Lidar Infrared Pathfinder Satellite Observations (CALIPSO) data: algorithm description, J. Atmos. Ocean. Tech., 26, 1105–1119, 2009.

Young, S. A., Vaughan, M. A., Kuehn, R. E., and Winker, D. M.: The retrieval of profiles of particulate extinction from Cloud-Aerosol Lidar Infrared Pathfinder Satellite Observations (CALIPSO) data: uncertainty and error sensitivity analyses", J. Atmos. Ocean. Tech., 30, 395–428, doi:10.1175/JTECH-D-12-00046.1, 2013.